applied sciences

MDPI

Article

Effect of CeO_2@GNPs on the Corrosion Properties of 2024 Alloy

Qingjie Wu [1,*], Zhenghua Guo [2], Junhua Cui [2], Liang Yang [2], Ning Li [2] and Surui Li [2]

[1] Key Laboratory for Microstructural Control of Metallic Materials of Jiangxi Province, Nanchang Hangkong University, Nanchang 330063, China
[2] Department of Materials Processing Engineering, School of Aeronautic Manufacturing Engineering, Nanchang Hangkong University, Nanchang 330036, China; guozh1972@163.com (Z.G.); cui@nchu.edu.cn (J.C.); l.yang@nchu.edu.cn (L.Y.); lining@nchu.edu.cn (N.L.); surui@nchu.edu.cn (S.L.)
* Correspondence: wu856200@163.com; Tel.: +86-0791-83863028

Abstract: The nanocomposites of 2024 Al reinforced with CeO_2@GNPs (graphene) nanoparticles were fabricated using the hot-press sintering method. With the addition of 0.5 wt% CeO_2@GNPs, the YS and UTS of the fabricated nanocomposites increased by 21.1% and 24.7%, respectively. The load transfer effect and optimization of the interfacial bonding were the main factors to improve the mechanical properties of the composites. The effect of the surface modification of GNPs on the corrosion resistance of the composites was investigated, demonstrating that the addition of GNPs weakened the corrosion resistance of the fabricated nanocomposites. Meanwhile, the corrosion current density (2.776×10^{-3} A·cm^{-2}) and polarization resistance (13,971.37 Ω cm^2) of the prepared composites with CeO_2 nanoparticle-layered GNPs exhibited a significant decreasing trend compared with the composites without a CeO_2 nanoparticle layer (3.540×10^{-3} A·cm^{-2}, 10,199.72 Ω cm^2). Optimizing the dispersion of GNPs and their interfacial bonding with the aluminum matrix promoted the reduction in the corrosion area and the possibility of micro-couple formation, leading to an effective enhancement of the corrosion resistance of the nanocomposites.

Keywords: aluminum matrix composites (AMCs); graphene nano-platelets; polarization resistance; corrosion current density

check for updates

Citation: Wu, Q.; Guo, Z.; Cui, J.; Yang, L.; Li, N.; Li, S. Effect of CeO_2@GNPs on the Corrosion Properties of 2024 Alloy. *Appl. Sci.* **2023**, *13*, 11775. https://doi.org/10.3390/app132111775

Academic Editor: Manoj Gupta

Received: 1 October 2023
Revised: 19 October 2023
Accepted: 26 October 2023
Published: 27 October 2023

Copyright: © 2023 by the authors. Licensee MDPI, Basel, Switzerland. This article is an open access article distributed under the terms and conditions of the Creative Commons Attribution (CC BY) license (https://creativecommons.org/licenses/by/4.0/).

1. Introduction

Aluminum alloys are utilized extensively in various industries, e.g., automotive and aerospace fields, due to their excellent attributes such as low density, improved formability as well as good electrical conductivity [1–3]. With the development of industry, aluminum alloy and its composites are expected to demonstrate higher mechanical properties and improved application performance [4,5]. Graphene nanoplatelets (GNPs) as a nanocarbon material have been gradually applied and modified with aluminum matrix composites (AMCs) in recent decades due to its high modulus of elasticity and tensile strength. Kumar AP et al. [6] reported the refinement of the grain and silicon phase of the A356 alloy due to GNPs incorporation via friction stir processing (FSP). Ju B et al. [7] prepared GNPs/Al composites using the pressure infiltration method and found that the interfacial shear strength of GNPs-Al_2O_3-Al was much higher than that of GNPs-Al, which further improved the mechanical properties of the composite. The relevant literature illustrates the fact that the incorporation of GNPs into aluminum alloys can effectively enhance the mechanical properties of the corresponding composites [8,9]. Surface modifications of GNPs can further enhance its strengthening properties for the metal alloy.

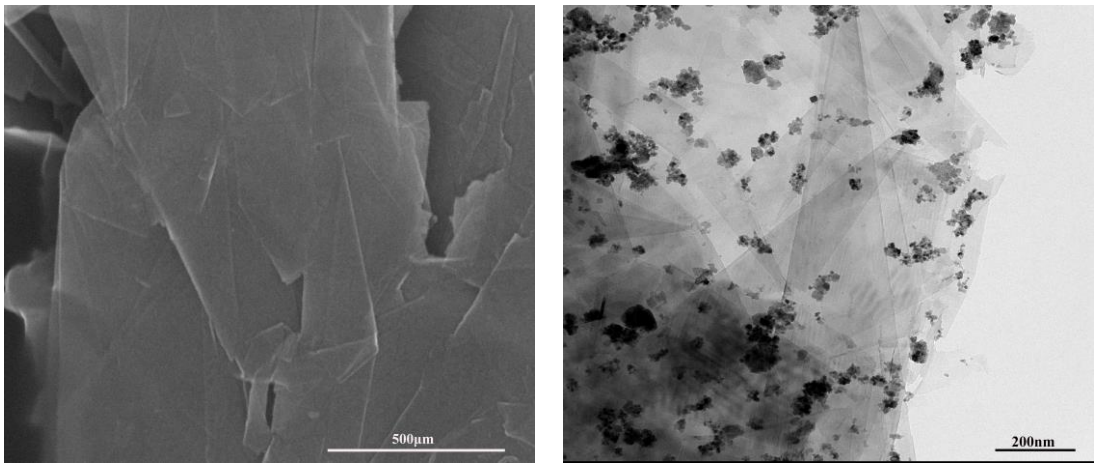
Recently, nanocarbon materials have often been surface coated and then used as an effective reinforcement in the development of AMCs by materials scientists. QH, Yuan et al. [10] prepared NiO@CNTs nano-reinforcements successfully and used them as the reinforcement for a Mg-4.0Zn alloy. The report concluded that the reinforcement of NiO@CNT had a better effect on the grain refinement and dispersion of the cast magnesium alloys

compared to the addition of raw CNTs. Qi, Lehua et al. reported that the improvement in the mechanical properties of the composites was mainly attributed to the good adherence at the interface between the Ni-CNTs and Mg matrix and no structural damage of the CNTs due to the presence of Ni coating [11,12]. These reports suggested that surface modification techniques are beneficial for improving the interfacial bonding of carbon nanomaterials with the matrix and enhancing the mechanical properties of the metal composites. In fact, most studies have mainly reported the structural and mechanical properties of AMCs reinforced with GNPs. However, one of the main reasons for the failure of the parts made of aluminum alloy is corrosion. The study of the corrosion properties of aluminum alloys is also crucial [13,14] apart from the mechanical properties. In the field of the corrosion resistance of metallic materials, engineers or researchers prefer to enhance the corrosion resistance of materials by coating their surfaces due to its high efficiency [15]. Few studies have provided insight into the corrosion behavior of those composites through the addition of reinforcements.

As we know, 2024 Al is widely used in aircraft skins, skeletons, truck hubs, propeller components and a variety of other structural components, where its mechanical properties and corrosion resistance play an important role in daily services. Therefore, it is necessary to study the corrosion behavior of aluminum matrix composites to ensure their reliability and safety during use. In the present study, the composites of 2024 Al reinforced with CeO_2@GNPs nanoparticles were fabricated using the hot-press sintering method. The intention was to strengthen the mechanical properties of the 2024 aluminum alloy while ensuring the effectiveness of its corrosion resistance. The reinforcement GNPs, on the other hand, were used to enhance their bonding to the matrix using surface-coated techniques. The mechanical properties and corrosion behavior were investigated for those composites and the matrix. Meanwhile, comparative experiments for the electrochemical properties were designed to investigate the influence of CeO_2 cladding on the corrosion behavior of the composites.

2. Materials and Methods

Materials Preparation: GNPs with a typical multilayer structure provided by Chengdu Zhongke Group were used as the starting materials to produce the reinforcement CeO_2@GNPs (Figure 1). The cladding preparation process was carried out using the alcohol–thermal cladding method, as described in Ref. [16]. The matrix material in this study was composed of a 2024 aluminum alloy powder provided by Hunan Tianjiu, (purity is 99.7%, 600~800 mesh in diameter), and its chemical composition is shown in Table 1.



(**a**) (**b**)

Figure 1. (**a**) SEM image of the graphene; (**b**) TEM image of the graphene with a CeO_2 nanoparticle layer.

Table 1. Chemical composition of the 2024 alloy (wt%).

Type	Cu	Mg	Fe	Si	Zn	Al
Wt pct	3.8~5.0	1.2~1.8	0.5	0.5	0.25	Bal.

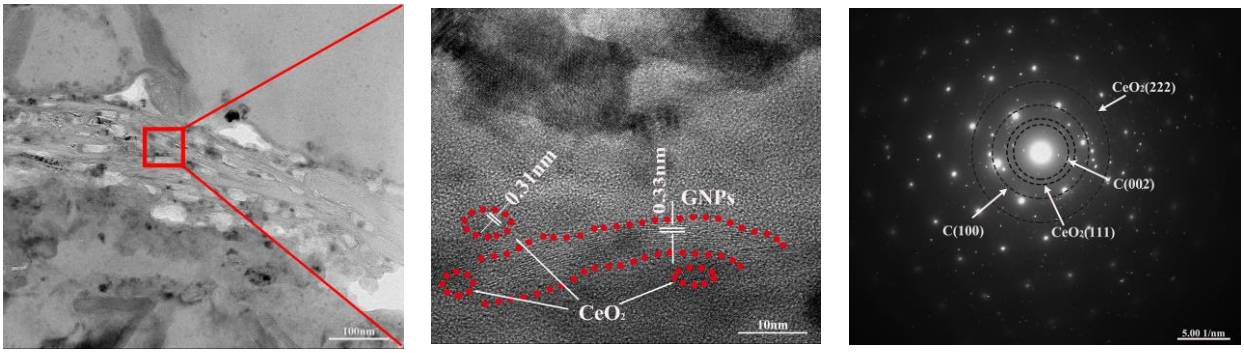
Preparation of the composites: The different types of GNPs and the as-received 2024 aluminum alloy powder were uniformly mixed using high-energy ball milling (HEBM) under an Ar atmosphere. This process was accomplished using a planetary ball mill with a grinding speed of 400 rpm for 2 h. Then, these mixed powders were added to the graphite mold in preparation for hot-press sintering. After degassing at 673 K, the mixed powder was compacted into φ 35 × 50 mm billets and consolidated using hot-press sintering under the conditions of vacuum of 3.9 × 10^{-3} Pa, a high temperature of 595 °C and pressure of 23 Mpa to obtain the desired material. The same process (milling, compaction and sintering) was used to prepare the 2024 alloy base material for comparison.

Corrosion test: The fabricated composites were cut into 10 × 10 × 3 mm squares for corrosion testing using wire electrical discharge machining. The electrochemical testing of these materials was performed in a 3.5% NaCl electrolyte at room temperature using the CHI604E electrochemical workstation. The corrosion samples were connected to the copper wires and encapsulated by epoxy resin, leaving an opening for contact with the reference electrode. The open-circuit potential (OCP) test was performed for 10 min, followed by the electrochemical impedance spectroscopy (EIS) test and the potential dynamic polarization curve Tafel test when the displayed data were stabilized. The frequency range of the impedance spectroscopy was 0.01 Hz–100 KHz, with a corresponding applied sinusoidal disturbance wave amplitude of 5 mV. The scanning range of the polarization curve was from EOCP −0.6 V to 0.6 V at a scan rate of 5 mV/s. The experimental data analysis was done in accordance with ASTM G5-14.

3. Results

3.1. Material Characterization

Figure 2 reveals the TEM and HRTEM analyses of the fabricated 0.5 wt% CeO_2@-GNPs/2024Al composites. The shape of the multilayer structure of the GNPs is clearly shown in Figure 2a,b, where the spacing of its level structures was approximately 0.33 nm. Additionally, the HRTEM image revealed the presence of some granular nanoparticles on the surface of the GNPs. The d-spacing provided by SAED were 0.16 nm and 0.31 nm, corresponding to the $(111)_{CeO2}$ crystal plane of the CeO_2 [17]. This phenomenon suggested that the layer of CeO_2 particles still remained at the GNPs surface after the hot isostatic pressing process preparation, which was useful for improving the bonding of the matrix with reinforcement as well as enhancing the mechanical properties of the prepared nanocomposites [18,19].



(**a**) (**b**) (**c**)

Figure 2. (**a**) TEM image of the graphene; (**b**) TEM image of the graphene with a CeO_2 nanoparticle layer; (**c**) Selected area electron diffraction of CeO_2 nanoparticle layer.

(SAED) pattern of Fe-Al phase particles

3.2. Mechanical Properties

Table 2 displays the tensile properties and microhardness of the matrix and fabricated nanocomposites with different types of GNPs. The strength and microhardness of the fabricated nanocomposites showed an increasing trend when two kinds of GNPs were added to the matrix, respectively. It was noticeable that the CeO_2@GNPs/2024Al nanocomposite exhibited a larger increase in the yield strength (YS) as well as ultimate tensile strength (UTS) than the GNPs/2024Al composite. The YS and UTS of the composite fabricated with 0.5 wt% CeO_2@GNPs were 184.1 and 271.8 MPa, increasing by 21.1% and 24.7% as compared to the matrix, respectively. The carbon-based reinforcement with coated particles was reported to impede the movement of dislocation in the composite during the deformation process [19]. Meanwhile, these reinforcing effects could also be attributed to the load transfer mechanism, which mainly referred to the load transfer from the matrix to the GNPs during the deformation process [20]. The theoretical values for increasing the YS of the nanocomposites due to the load transfer effect could be calculated via the Kelly–Tyson formula.

$$\Delta\sigma_{LT} = \frac{f_v}{2}\sigma_m \quad (1)$$

where is the volume fraction of the GNPs. denotes the YS of the matrix. Typically, the increment of YS obtained through the theoretical calculation mentioned above is much larger than the actual increment value. The key to the reduction in disparity is the optimization of the interface wettability between the GNPs and the matrix as well as its dispersion in the matrix [20,21]. In this study, the existence of CeO_2 nanoparticles on the surfaces of the GNPs was beneficial for dispersing the GNPs uniformly and the interfacial wettability. Thus, it led to a further improvement in the mechanical properties of the composites.

Table 2. Mechanical properties of the fabricated composites.

Materials	Ys/MPa	UTs/MPa	EI (%)	Microhardness (HV)
Matrix	152 ± 5	218 ± 6	2.77 ± 0.19	101.2 ± 3.2
GNPs/2024Al nanocomposite	170.6 ± 5	257.4 ± 6.4	2.53 ± 0.23	111 ± 4.8
CeO_2@GNPs/2024Al nanocomposite	184.1 ± 4.7	271.8 ± 3.8	2.38 ± 0.34	128 ± 5.9

3.3. Corrosion Resistance

The morphologies of the 2024 Al alloy, 0.5 wt%GNPs/2024Al and 0.5 wt%CeO_2@-GNPs/2024Al soaked in a 3.5 wt% NaCl solution for seven days are given in Figure 3. It can be observed that the surfaces of the samples were all covered by white flaky corrosion products or bright corrosion particles, which were presumed to be Al_2O_3, $Al(OH)_3$ and $Mg(OH)_2$ particles when using the EDS energy spectrum analysis and the characteristic peaks in the XRD patterns, as shown in Figure 3f [17]. However, the XRD patterns collected from those composites reinforced with the GNPs specimens did not reveal any peaks of GNPs. The reason for this may have been the low concentration of GNPs in the matrix. Additionally, the surface of the 0.5 wt%CeO_2@GNPs/2024Al specimen showed fewer deposits compared to the 0.5 wt%GNPs/2024Al sample.

Figure 4 shows the mapping images of the different elements in the 0.5 wt% GNPs/2024Al composite sample. It can be observed that the pitting crater with a diameter of approx. 40 μm at P1 was accompanied by the generation of surface corrosion products as well as an oxide film in the process of pitting corrosion generation. As the corrosion continued, the passivation film on the surface was broken through and corrosion cracks sprouted and extended continuously. Therefore, it could be noticed that the Cu elements and Cl elements had only a small distribution

on the corrosion surface. On the other hand, a small number of new corrosion cracks were generated under the corrosion cracks, indicating that the generation of pitting corrosion entered a new phase and continued to expand. In addition, it can be clearly observed from Figure 4 that the Al elements and O elements were widely distributed on the surface-covered corrosion products, while the Mg elements were mainly distributed along the corrosion product particles. This implies that one of the main components of the corrosion product was the Mg element.

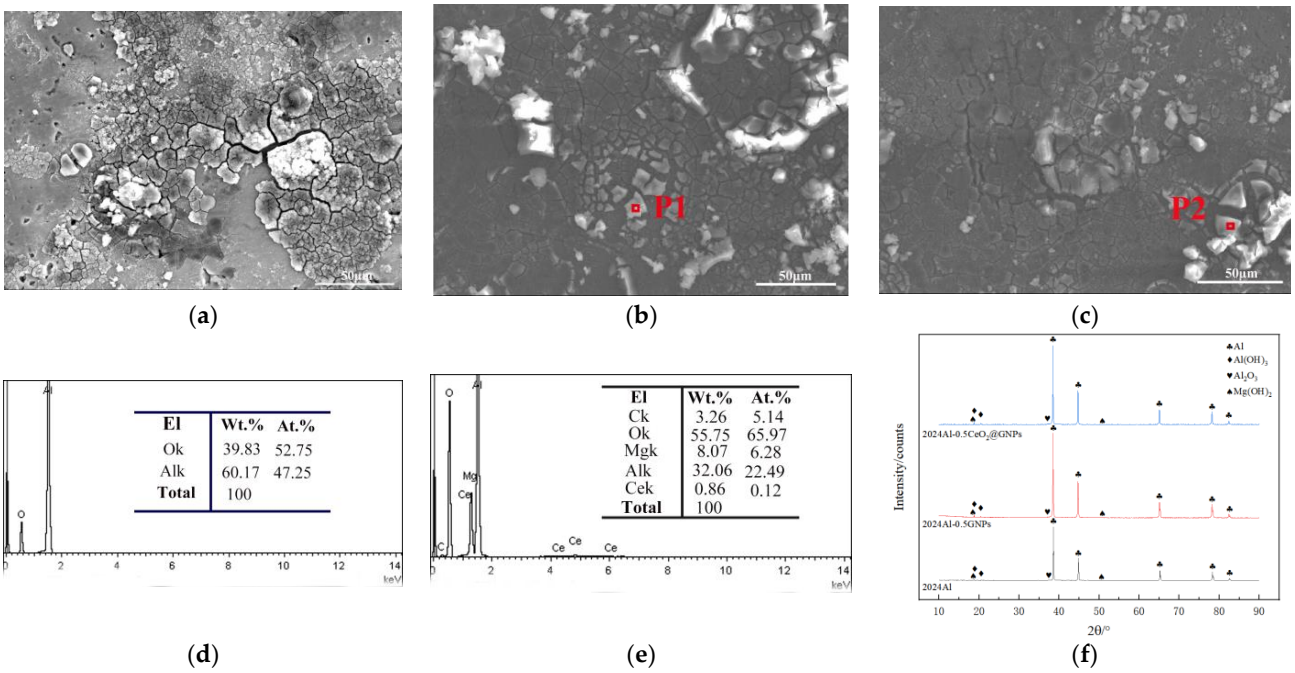


Figure 3. SEM maps and energy spectra of the corrosion morphology of the 2024 aluminum alloy and its nanocomposites: (**a**) SEM map of the 2024 aluminum alloy, (**b**) SEM map of the 0.5 wt%GNPs/2024Al nanocomposites, (**c**) SEM map of the 0.5 wt%CeO_2@GNPs/2024Al nanocomposites; (**d**) P1 point energy spectrum; (**e**) P2 point energy spectrum; (**f**) XRD patterns of the nanocomposites.

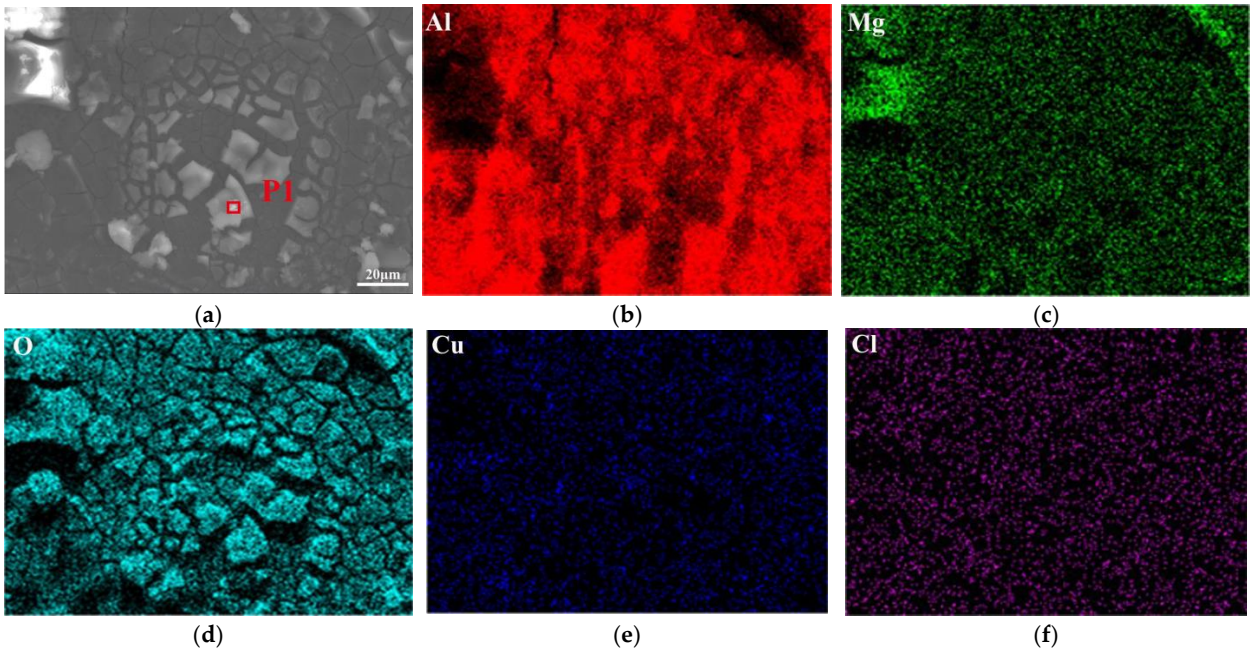


Figure 4. Distribution of the scanning elements in the area shown in Figure 3 (**a**). (**b**) Al; (**c**) Mg; (**d**) O; (**e**) Cu; (**f**) Cl.

Figure 5a displays the electrochemical parameters obtained using Tafel curve fitting. The OCP curves of three different samples exhibited the same trend as could been seen from Figure 5a. All the curves showed only positive fluctuations at first, gradually decreased and tended to stabilize around a certain value. This phenomenon mainly indicated that the sample surface passivation layers were rapidly destroyed. Meanwhile, due to the continuous formation of oxide, a dynamic equilibrium between local corrosion and oxide film formation was promoted, which led to the gradual stabilization of the potential curve. It is worth noting that the OCP profile of the fabricated 0.5 wt%CeO_2@GNPs/2024Al nanocomposite took more time to reach a stable state compared to the others and that this specimen had the highest open-circuit potential after stabilization. This illustrates that the 0.5 wt%CeO_2@GNPs-2024Al nanocomposite had the lowest tendency to be corroded compared to the other two materials [22,23].

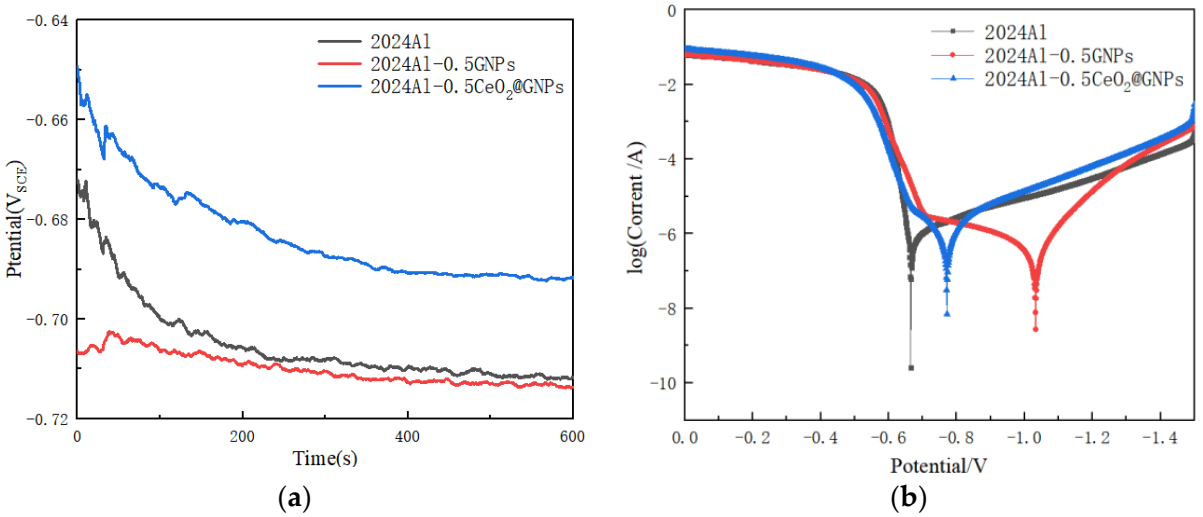


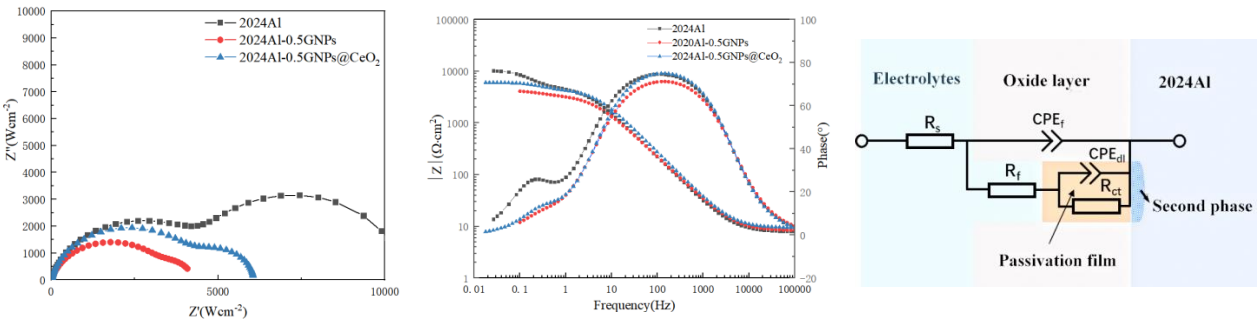
Figure 5. Open-circuit potential curves and potentiodynamic polarization curves for the 2024 aluminum alloys and their nanocomposites: (**a**) OCP curves; (**b**) Tafel curves.

The polarization curves of the different samples in a corrosive solution of 3.5 wt% NaCl prepared from a plating bath are shown in Figure 5b. Correspondingly, the extracted data of the entire Tafel curve are shown in Table 3. It can be seen that the matrix of the 2024 Al alloy had the highest corrosion potential (Ecorr) and the lowest corrosion current density (Icorr). The specimens of the 0.5 wt%GNPs-2024Al nanocomposite exhibited a lower Ecorr and a higher Icorr compared to the matrix, indicating that the addition of GNPs weakened the corrosion resistance of the fabricated nanocomposite. This was mainly attributed to agglomerated GNPs in the matrix, which became cathodic sites and resulted in the galvanic corrosion of the nanocomposites [24,25]. Meanwhile, it can also be seen from Figure 5b that the Ecorr increased and the Icorr decreased after adding 0.5 wt%CeO_2@GNPs, indicating that the existence of the CeO_2 layer improved the corrosion resistance to some extent compared to the 0.5 wt%GNPs/2024Al [26].

Table 3. Tafel curve parameters for the different materials.

Specimen	E_{corr} (V_{SCE})	I_{corr} ($A \cdot cm^{-2}$)
Matrix	−0.665	2.757×10^{-3}
GNPs/2024Al nanocomposite	−1.03	3.540×10^{-3}
CeO_2@GNPs/2024Al nanocomposite	−0.772	2.776×10^{-3}

The Nyquist and Bode plots obtained through fitting using the ZsimpWin 3.6 software are shown in Figure 6. It was evident that the specimens were composed of two capacitive arcs, a high frequency and a low and medium frequency. The Nyquist plots of the 0.5 wt%CeO_2@GNPs/2024Al and 0.5 wt%GNPs/2024Al nanocomposites within the investigated range of frequencies had a similar trajectory. Additionally, a larger diameter of the capacitive loop in the 0.5 wt%CeO_2@GNPs/2024Al compared with the 0.5 wt%GNPs/2024Al nanocomposite signified a higher resistance to corrosion [27].



(**a**) (**b**) (**c**)

Figure 6. EIS curves and the equivalent circuit diagrams for the 2024 aluminum alloy and its nanocomposites: (**a**) Nyquist diagram; (**b**) Bode diagram; (**c**) equivalent electrical circuit.

Table 4 exhibits the related EC fitted parameters. The polarization resistance (R_p) could be calculated using Equation (2) as follows [28].

$$R_p = R_s + R_f + R_{ct} \quad (2)$$

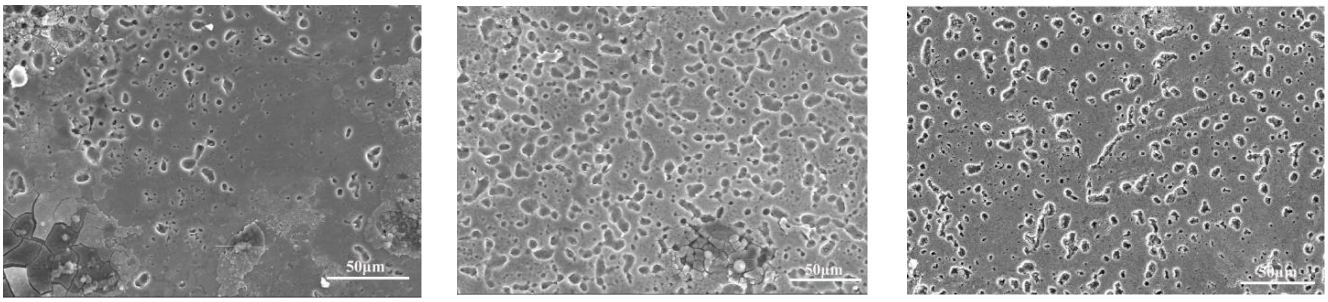
where R_s is the electrolyte resistance, which is related to the conductivity of the electrolyte. R_f is the oxide layer resistance. R_{ct} represents the oxide charge transfer resistance. CPE_f and CPE_{dl} are the capacitances of the oxide film and the double layer, respectively. They are usually associated with cracks, surface oxide films, impurities and inhomogeneous distribution. The calculation results according to Table 4 demonstrated that the R_p of those fabricated nanocomposites were significantly lower than that of the matrix 2024 Al alloy (21,168 Ω). The matrix 2024 Al alloy suffered a decrease in the corrosion resistance of the surface oxide layer as well as the internal matrix due to the addition of GNPs. Additionally, the surface modification of GNPs using the attached CeO_2 nanoparticles improved the corrosion resistance of the material and partially eliminated the effect of GNPs on the corrosion resistance damage of aluminum-based materials.

Table 4. Electrochemical impedance spectral parameters of the different specimens.

Materials	R_s ($\Omega \cdot cm^2$)	CPE_f		R_f ($\Omega \cdot cm^2$)	CPE_{dl}		R_{ct} ($\Omega \cdot cm^2$)
		$Y0_f$ ($\Omega^{-1} \cdot cm^{-2} \cdot s^n$)	n_f		Y0 ($\Omega^{-1} \cdot cm^{-2} \cdot s^n$)	n	
Matrix	22.18	15.7×10^{-6}	0.88	10,569	2.3×10^{-4}	0.97	10,577
2024Al-0.5GNPs	22.39	18.6×10^{-6}	0.85	7244.85	8.4×10^{-4}	0.97	2932.48
2024Al-0.5GNPs@CeO_2	22.76	11.8×10^{-6}	0.89	9251.39	4.2×10^{-4}	0.96	4697.22

The SEM images of the matrix and the fabricated nanocomposite after the removal of the corrosion products are shown in Figure 7. It can be clearly observed that the smooth surfaces of the specimens were characterized by a large number of corrosion pits and corrosion micropores. The 0.5 wt%GNPs/2024Al specimen was subjected to more severe corrosion than the matrix, which was almost completely covered by corrosion pits. Some of the corrosion pits were connected to the presence of larger sized corrosion pits. On the other hand, the corrosion surface of the 0.5 wt%CeO_2@GNPs/2024Al nanocomposite presented

fewer corrosion pits with smaller diameters compared to the former. These phenomena demonstrated that the addition of raw GNPs accelerated the corrosion behavior of aluminum alloys and further proved the corrosion inhibition ability of the CeO_2 nanoparticles layer. The overall corrosion mechanism was governed by the reactions below [29].



(**a**) (**b**) (**c**)

Figure 7. SEM images of the 2024 Al alloy and its nanocomposites with the removal of the surface corrosion products: (**a**) 2024 Al alloy; (**b**) 0.5 wt%GNPs/2024Al nanocomposite; (**c**) 0.5 wt%CeO_2@GNPs/2024Al nanocomposite.

The anodic reactions can be written as follows.

$$Mg \rightarrow Mg^{2+} + 2e^- \quad (3)$$

$$Al \rightarrow Al^{3+} + 3e^- \quad (4)$$

The cathodic reaction can be written as follows.

$$O_2 + 2H_2O + 4e^- \rightarrow 4OH^- \quad (5)$$

The overall reaction occurred as follows.

$$2Mg + O_2 + 2H_2O \rightarrow 2Mg(OH)_2 \quad (6)$$

$$4Al + 3O_2 + 6H_2O \rightarrow 4Al(OH)_3 \quad (7)$$

$$2Al(OH)_3 \rightarrow Al_2O_3 + 3H_2O \quad (8)$$

The corrosion types of the composites were similar to those of the matrix 2024 Al alloy, dominated by pitting and intergranular corrosion. With the increase in the immersion time, the oxide films of those were gradually destroyed (Figure 8). The GNPs had a structure similar to that of unfolded carbon nanotubes and had similar physical properties. There was a large surface potential difference between the GNPs and α-Al [30,31]. Therefore, the GNPs phase acted as a cathodic phase and the micro-coupled corrosion of the α-Al phase, which contributed to the depletion of the α-Al phase in the vicinity of the GNPs and the generation of white corrosion products (micro-coupling corrosion). Eventually, more severe localized corrosion occurred near the added GNPs enhanced phase [24]. Compared with agglomerated GNPs, the dispersed GNPs generated more micro-couples, leading to more severe micro-coupling corrosion. Furthermore, the inhomogeneous dispersion of the GNPs may have decreased the diffusivity of O ions [32], which resulted in an insufficiently dense oxide film. The oxide film was poorly resistant to corrosive fluid erosion and was prone to rupture and collapse, thus leading to the occurrence of pitting corrosion.

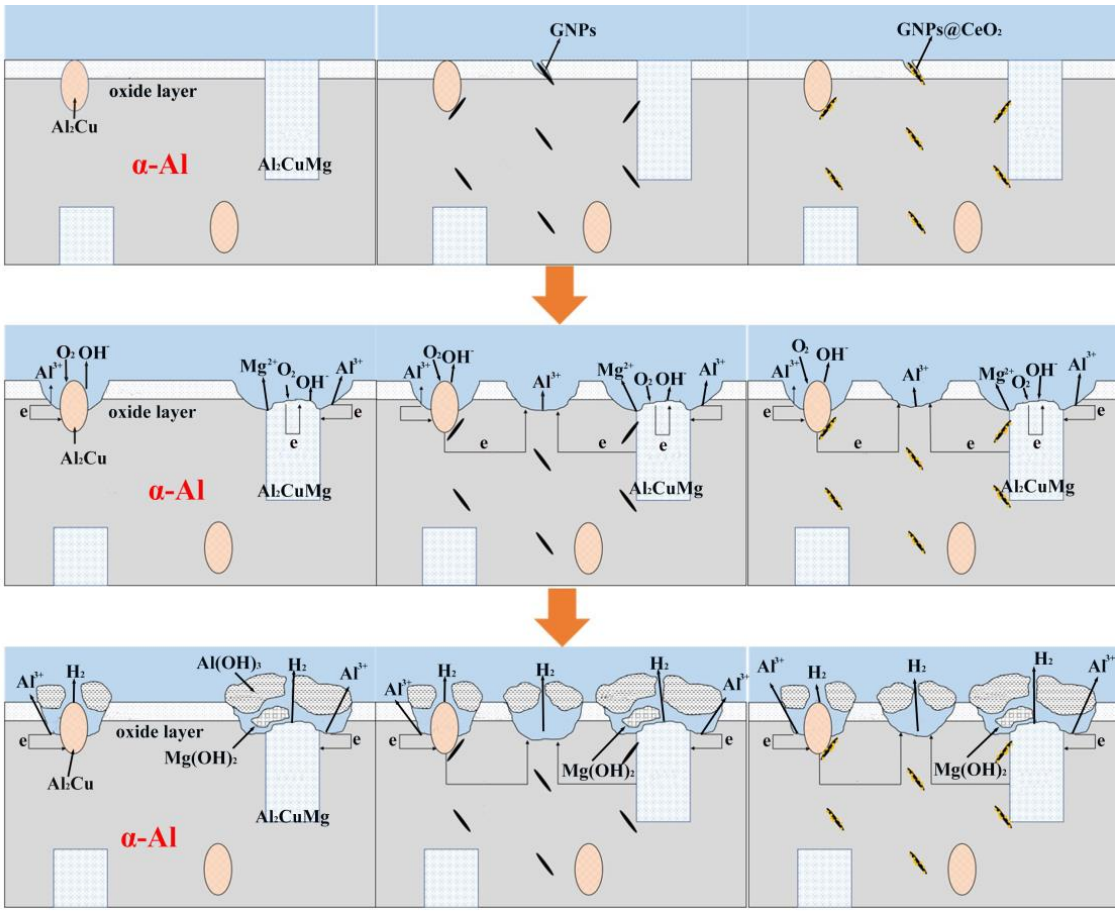


Figure 8. Sketch of the corrosion principle of the nanocomposites in a NaCl solution.

On the other hand, the poor interfacial bonding properties between the GNPs and the Al matrix resulted in the presence of defects, such as pores and cracks in the composites [33], which disrupted the integrity of the surface oxide film and allowed the NaCl electrolyte to bypass the surface oxide layer and react directly with the α-Al. The corrosion resistance of the 0.5 wt%CeO_2@GNPs/2024Al nanocomposite was improved compared to the previous sample. The CeO_2 modification of the GNPs surface was equivalent to the surface coating of a layer of CeO_2 ceramic phase passivation film, which impeded the galvanic coupling corrosion behavior between the GNPs and α-Al. Moreover, it was shown that CeO_2 nanoparticles could react weakly with aluminum to form trace amounts of Al_4Ce intermediate grains [34–36], which promoted wetting bonding with the matrix. This reduced the microporosity due to the agglomeration of GNPs or the poor binding properties of the matrix, reducing the corrosion area and improving the corrosion resistance of the composites. The existence of CeO_2 refined the grains and improved the densities of the materials, thus improving the corrosion resistance of the nanocomposites.

4. Conclusions

1. The YS and UTS of the 0.5 wt% CeO_2@GNPs nanocomposite fabricated using the hot-press sintering method were 21.1% and 24.7% higher than the matrix, respectively. The existence of CeO_2 nanoparticles on the surfaces of the GNPs led to a further improvement in the mechanical properties of the composites.
2. The addition of raw GNPs weakened the corrosion resistance. However, the corrosion current density (2.776×10^{-3} A·cm^{-2}) and polarization resistance (13,971.37 Ω cm^2) with CeO_2 nanoparticle-layered GNPs exhibited a significant decreasing trend compared to the nanocomposites without CeO_2 (3.540×10^{-3} A·cm^{-2}, 10,199.72 Ω cm^2).

3. The corrosion types of sintered matrix, nanocomposites reinforced with 0.5 wt% GNPs and CeO_2 modified GNPs in a 3.5 wt% NaCl solution were dominated by pitting and intergranular corrosion. The presence of GNPs in the composite destroyed the integrity of the oxide film on the surface of the material. The potential of the GNPs was higher than that of the Al matrix, which constituted a micro-coupled corrosion and accelerated the dissolution of Al. The presence of the corrosion inhibitor CeO_2 particles on the surface of the GNPs acted as a passivation film to impede the charge transfer. It improved the interfacial bonding between the reinforcement and the Al matrix, which reduced the generation of microcracking and contributed to the improved corrosion resistance of the nanocomposites.

Author Contributions: Conceptualization, Q.W. and Z.G.; writing, Q.W.; formal analysis and data curation, J.C. and L.Y.; funding acquisition, N.L. and S.L. All authors have read and agreed to the published version of the manuscript.

Funding: This research was funded by the Jiangxi Provincial key laboratory open fund project, grant number "EJ202003431" and Key R&D Projects in Jiangxi Province, grant number "20192BBE50002".

Institutional Review Board Statement: Not applicable.

Informed Consent Statement: Not applicable.

Data Availability Statement: The data from this experiment are not published in other journals or databases at this time.

Conflicts of Interest: The authors declare no conflict of interest.

References

1. Conde, A.; de Damborenea, J. Evaluation of exfoliation susceptibility by means of the electrochemical impedance spectroscopy. *Corros. Sci.* **2000**, *42*, 1363–1377. [CrossRef]
2. Prasad, S.D.; Krishna, R.A. Production and mechanical properties of A356.2/RHA composites. *Int. J. Adv. Sci. Technol.* **2011**, *33*, 51–58.
3. Konieczny, J.; Labisz, K.; Dolata, A.J. Structure and Functional Properties of Surface Layer Produced on Cast Aluminium Light Alloys by Appliance of Anodisation. *Solid State Phenom.* **2015**, *229*, 51–56.
4. Chen, M.Q.; Bai, Y.L.; Zhang, Z.F. Research Progress on Preparation of SiC/Al for Electronic Packaging by Liquid Infiltration. *Mater. Sci. Forum* **2021**, *1035*, 906–917.
5. Alizadeh, M.; Shakery, A.; Salahinejad, E. Aluminum-matrix composites reinforced with E-glass fibers by cross accumulative roll bonding process. *J. Alloys Compd.* **2019**, *804*, 450–456. [CrossRef]
6. Kumar, P.A.; Madhu, H.C.; Pariyar, A.; Perugu, C.S.; Kailas, S.V.; Garg, U.; Rohatgi, P. Friction stir processing of squeeze cast A356 with surface compacted graphene nanoplatelets (GNPs) for the synthesis of metal matrix composites. *Mater. Sci. Eng.* **2020**, *769*, 138517. [CrossRef]
7. Ju, B.; Yang, W.; Shao, P.; Hussain, M.; Zhang, Q.; Xiu, Z.; Hou, X.; Qiao, J.; Wu, G. Effect of Interfacial Microstructure on the Mechanical Properties of GNPs/Al Composites. *Carbon* **2020**, *162*, 346–355. [CrossRef]
8. Sharma, A.; Sharma, V.M.; Sahoo, B.; Pal, S.K.; Paul, J. Effect of multiple micro channel reinforcement filling strategy on A16061-graphene nanocomposite fabricated through friction stir processing. *J. Manuf. Process.* **2019**, *37*, 53–70. [CrossRef]
9. Sharma, A.; Sharma, V.M.; Jinu, P.A.U.L. A comparative study on microstructural evolution and surface properties of graphene/CNT reinforced Al6061-SiC hybrid surface composite fabricated via friction stir processing. *Trans. Nonferrous Met. Soc. China* **2019**, *29*, 2005–2026. [CrossRef]
10. Yuan, Q.; Zeng, X.; Wang, Y.; Luo, L.; Ding, Y. Microstructure and mechanical properties of Mg-4.0Zn alloy reinforced by NiO-coated CNTs. *J. Mater. Sci. Technol.* **2017**, *33*, 452–460. [CrossRef]
11. Carvalho, S.S.N.D. Mechanical, Fatigue and Wear Properties of Sintered Carbon Nanotube-Based Functionally Graded Materials. Ph.D. Thesis, Universidade do Minho (Portugal), Braga, Portugal, 2015.
12. Liang, J.; Li, H.; Qi, L.; Tian, W.; Li, X.; Zhou, J.; Wang, D.; Wei, J. Influence of Ni-CNTs additions on the microstructure and mechanical properties of extruded Mg-9Al alloy. *Mater. Sci. Eng. A Struct. Mater. Prop. Misrostructure Process.* **2016**, *678*, 101–109. [CrossRef]
13. Huang, J.; Meng, X.; Huang, Y.; Jiang, W.; Chen, R.; Zheng, Z.; Gao, Y. Atmospheric corrosion of carbon steels in tropical and subtropical climates in Southern China. *Mater. Corros.* **2020**, *71*, 1400–1406. [CrossRef]
14. Egorkin, V.S.; Medvedev, I.M.; Sinebryukhov, S.L.; Vyaliy, I.E.; Gnedenkov, S.V. Atmospheric and Marine Corrosion of PEO and Composite Coatings Obtained on Al-Cu-Mg Aluminum Alloy. *Materials* **2020**, *13*, 2739–2964. [CrossRef] [PubMed]

15. Sobolev, A.; Bograchev, D.; Borodianskiy, K.; Zinigrad, M. Kinetics and mechanism of corrosion of oxide coating fabricated on aluminum alloy by the plasma electrolytic oxidation in molten salt. *Corros. Sci. J. Environ. Degrad. Mater. Control* **2022**, *208*, 96–110.
16. Guo, Z.H.; Li, S.; Wu, Q.; Li, N. Rare Earth Oxide CeO_2 Decorated Graphene Nanoplatelets-Reinforced 2024 Aluminum Alloy Matrix Composites Fabricated by Pressure Sintering Process. *Appl. Sci.* **2021**, *11*, 11177. [CrossRef]
17. JCPDS, International Centre for Diffraction Data, PCDFWIN. 2002. Available online: https://www.scirp.org/(S(vtj3fa45qm1ean45vvffcz55))/reference/referencespapers.aspx?referenceid=1856390 (accessed on 30 September 2023).
18. Ran, Q.; Yan, H.; He, J.; Li, N.; Lei, Y. Effect of TiO_2@Carbon Nanotubes and Praseodymium on the Microhardness and Corrosion Properties of AZ91 Alloy. *Met. Mater. Int.* **2022**, *28*, 2012–2022. [CrossRef]
19. Li, N.; Yan, H.; Wu, Q. Fabrication of Carbon Nanotubes and Rare Earth Pr Reinforced AZ91 Composites by Powder Metallurgy. *Chin. J. Mech. Eng.* **2021**, *2*, 213–222. [CrossRef]
20. Rashad, M.; Pan, F.; Tang, A.; Asif, M.; Hussain, S.; Gou, J.; Mao, J.J. Improved strength and ductility of magnesium with addition of aluminum and graphene nanoplatelets (Al+GNPs) using semi powder metallurgy method. *J. Ind. Eng. Chem.* **2015**, *23*, 243–250. [CrossRef]
21. Wang, Y.; Zhu, C.; Lei, T. Preparation and properties of graphene reinforced aluminum matrix composites. *Mater. Sci. Eng. Powder Metall.* **2018**, *23*, 518–526.
22. Cheng, D.; Zhang, L.; Zhan, Z.; Xia, H.; Ma, K.; Ma, H.; Gao, Y. Preparation and Properties of Ni–W Composite Coatings Reinforced by Graphene Nanoplatelets. *Adv. Eng. Mater.* **2021**, *23*, 2001309. [CrossRef]
23. Tao, S.; Li, D.Y. Tribological, mechanical and electrochemical properties of nanocrystalline copper deposits produced by pulse electrodeposition. *Nanotechnology* **2006**, *17*, 65–78. [CrossRef]
24. Shahin, M.; Wen, C.; Munir, K.; Li, Y. Mechanical and corrosion properties of graphene nanoplatelet–reinforced Mg–Zr and Mg–Zr–Zn matrix nanocomposites for biomedical applications. *J. Magnes. Alloys* **2022**, *10*, 458–477. [CrossRef]
25. Rashad, M.; Pan, F.; Yu, Z.; Asif, M.; Lin, H.; Pan, R. Investigation on microstructural, mechanical and electrochemical properties of aluminum composites reinforced with graphene nanoplatelets. *Prog. Nat. Sci. Mater. Int.* **2015**, *25*, 460–470. [CrossRef]
26. Yu, B.; Yan, H.; Wu, Q.; Hu, Z.; Chen, F.H. Microstructure and corrosion behavior of Al3Ti/ADC12 composite modified with Sr. *Int. J. Miner. Metall. Mater.* **2018**, *25*, 840–848. [CrossRef]
27. Xie, Y.; Meng, X.; Mao, D.; Qin, Z.; Wan, L.; Huang, Y.X. Homogeneously Dispersed Graphene Nanoplatelets as Long-Term Corrosion Inhibitors for Aluminum Matrix Composites. *ACS Appl. Mater. Interfaces* **2021**, *13*, 32161–32174. [CrossRef] [PubMed]
28. Lai, T.; Yin, Z.; Shen, J.; Sun, P.F.; Liu, Q.; Wang, K.; Yan, H.; Song, H.; Luo, C.; Hu, Z. Effects of SnO_2 Passive Film and Surface Micro-Galvanic Corrosion on the Corrosion Behavior of as-Extruded Mg-9Li-5Al-xSn Alloys. *J. Electrochem. Soc.* **2021**, *168*, 81502. [CrossRef]
29. Munir, K.; Wen, C.; Li, Y. Graphene nanoplatelets-reinforced magnesium metal matrix nanocomposites with superior mechanical and corrosion performance for biomedical applications. *J. Magnes. Alloys* **2020**, *8*, 269–290. [CrossRef]
30. Schujman, S.B.; Vajtai, R.; Shusterman, Y.; Biswas, S.; Dewhirst, B.; Schowalter, L.J.; Wei, B.Q.; Ajayan, P.M. AFM-Based Surface Potential Measurements on Carbon Nanotubes. *MRS Proc.* **2001**, *706*, 377–382. [CrossRef]
31. Fratila-Apachitei, L.E.; Apachitei, I.; Duszczyk, J. Characterization of cast AlSi(Cu) alloys by scanning Kelvin probe force microscopy. *Electrochim. Acta* **2006**, *51*, 5892–5896. [CrossRef]
32. Wei, Z.; Yan, H.; Huang, Z.; Wu, Q.; Zou, Y. Processing and Properties of CNTs/ADC12 Nanocomposite. *J. Mater. Eng. Perform.* **2018**, *27*, 6737–6747. [CrossRef]
33. Chang, C.H.; Huang, T.C.; Peng, C.W.; Yeh, T.C.; Lu, H.I.; Hung, W.I.; Weng, C.J.; Yang, T.I.; Yeh, J.M. Novel anticorrosion coatings prepared from polyaniline/graphene composites. *Carbon* **2012**, *50*, 5044–5051. [CrossRef]
34. Skrzekut, T.; Kula, A.; Blaz, L.; Sugamata, M. Structural Characterization of Mechanically Alloyed AlMg-CeO_2 Composite. *Key Eng. Mater.* **2015**, *641*, 10–16.
35. Skrzekut, T.; Kula, A.; Blaz, L.; Sugamata, M. High-Strength and Thermally Stable Al-CeO2 Composite Produced by Means of Mechanical Alloying. *Int. J. Mater. Res.* **2014**, *105*, 282–287. [CrossRef]
36. Zhiguo, D.; Guangchun, Y.; Yihan, L.; Luo, T.; Li, H. Preparation and Characterization of Graphite Powder Covered with CeO_2. *Int. Conf. Rare Earth Res. Appl.* **2006**, *24*, 57–60. [CrossRef]

Disclaimer/Publisher's Note: The statements, opinions and data contained in all publications are solely those of the individual author(s) and contributor(s) and not of MDPI and/or the editor(s). MDPI and/or the editor(s) disclaim responsibility for any injury to people or property resulting from any ideas, methods, instructions or products referred to in the content.